Technical University of Denmark

DTU

Optical Cherenkov radiation in an As2S3 slot waveguide with four zero-dispersion wavelengths

Wang, Shaofei; Hu, Jungao; Guo, Hairun; Zeng, Xianglong

Link back to DTU Orbit

DTU Library
Technical Information Center of Denmark

Optical Cherenkov radiaton in an As_2S_3 slot waveguide with four zero-dispersion wavelengths

Shaofei Wang,[1] Jungao Hu,[1] Hairun Guo,[2] and Xianglong Zeng[1,2,*]

[1]*The Key Lab of Specialty Fiber Optics and Optical Access Network, Shanghai University, 200072 Shanghai, China*
[2]*Department of Photonics Engineering,Technical University of Denmark, DK-2800 Kgs. Lyngby, Denmark*

[*]zenglong@shu.edu.cn

Abstract: We propose an approach for an efficient generation of optical Cherenkov radiation (OCR) in the near-infrared by tailoring the waveguide dispersion for a zero group-velocity mismatching between the radiation and the pump soliton. Based on an As_2S_3 slot waveguide with subwavelength dimensions, dispersion profiles with four zero dispersion wavelengths are found to produce a phase-matching nonlinear process leading to a broadband resonant radiation. The broadband OCR investigated in the chalcogenide waveguide may find applications in on-chip wavelength conversion and near-infrared pulse generation.

OCIS codes: (190.5530) Pulse propagation and temporal solitons; (190.7110) Ultrafast nonlinear optics.

References and links

1. J. Ranka, R. Windeler, and A. Stentz, "Visible continuum generation in air-silica microstructure optical fibers with anomalous dispersion at 800 nm," Opt. Lett. **25**, 25–27 (2000).
2. I. Cristiani, R. Tediosi, L. Tartara, and V. Degiorgio, "Dispersive wave generation by solitons in microstructured optical fibers," Opt. Express **12**, 124–135 (2004).
3. D. R. Austin, C. M. de Sterke, B. J. Eggleton, and T. G. Brown, "Dispersive wave blue-shift in supercontinuum generation," Opt. Express **14**, 11997–12007 (2006).
4. J. M. Dudley, G. Genty, and S. Coen, "Supercontinuum generation in photonic crystal fiber," Rev. Mod. Phys. **78**, 1135–1184 (2006).
5. D. V. Skryabin, F. Luan, J. C. Knight, and P. St. J. Russell, "Soliton self-frequency shift cancellation in photonic crystal fibers," Science **301**, 1705–1708 (2003).
6. H. Tu and S. A. Boppart, "Optical frequency up-conversion by supercontinuum-free widely-tunable fiber-optic Cherenkov radiation," Opt. Express **17**, 9858–9872 (2009).
7. N. Akhmediev and M. Karlsson, "Cherenkov radiation emitted by solitons in optical fibers," Phys. Rev. A **51**, 2602–2607 (1995).
8. S. Roy, D. Ghosh, S. K. Bhadra, and G. P. Agrawal, "Role of dispersion profile in controlling emission of dispersive waves by solitons in supercontinuum generation," Opt. Commun. **283**, 3081–3088 (2010).
9. M. R. E. Lamont, B. Luther-Davies, D. Choi, S. Madden, and B. J. Eggleton, " Supercontinuum generation in dispersion engineered highly nonlinear ($\gamma = 10/W/m$) As_2S_3 chalcogenide planar waveguide," Opt. Express **16**, 14938–14944 (2008).
10. C. Xiong, E. Magi, F. Luan, A. Tuniz, S. Dekker, J. S. Sanghera, L. B. Shaw, I. D. Aggarwal, and B. J. Eggleton, "Characterization of picosecond pulse nonlinear propagation in chalcogenide As_2S_3 fiber," Appl. Opt. **48**, 5467–5474 (2009).
11. J. T. Gopinath, M. Soljacic, E. P. Ippen, V. N. Fuflyigin, W. A. King, and M. Shurgalin, "Third order nonlinearities in Ge-As-Se-based glasses for telecommunications applications," J. Appl. Phys. **96**, 6931-6933 (2004).
12. I. W. Hsieh, X. G. Chen, X. P. Liu, J. I. Dadap, N. C. Panoiu, C. Y. Chou, F. N. Xia, W. M. Green, Y. A. Vlasov, and R. M. Osgood, "Supercontinuum generation in silicon photonic wires," Opt. Express **15**, 15242–15249 (2007).

13. L. Zhang, Q. Lin, Y. Yue, Y. Yan, R. G. Beausoleil, and A. E. Willner, "Silicon waveguide with four zero-dispersion wavelengths and its application in on-chip octave-spanning supercontinuum generation," Opt. Express **20**, 1685–1690 (2012).
14. V. R. Almeida, Q. F. Xu, C. A. Barrios, and M. Lipson, "Guiding and confining light in void nanostructure," Opt. Lett. **29**, 1209-1211 (2004).
15. S. Mas, J. Caraquitena, J. V. Galán, P. Sanchis, and J. Martí, "Tailoring the dispersion behavior of silicon nanophotonic slot waveguides," Opt. Express **18**, 20839–20844 (2010).
16. M. Zhu, H. J. Liu, X. F. Li, N. Huang, Q. B. Sun, J. Wen, and Z. L. Wang, "Ultrabroadband flat dispersion tailoring of dualslot silicon waveguides," Opt. Express **20**, 15899–15907 (2012).
17. V. G. Ta'eed, N. J. Baker, L. Fu, K. Finsterbusch, M. R. E. Lamont, D. J. Moss, H. C. Nguyen, B. J. Eggleton, D. Y. Choi, S. Madden, and B. Luther-Davies, "Ultrafast all-optical chalcogenide glass photonic circuits," Opt. Express **15**, 9205–9221 (2007).
18. B. Kibler, P.-A. Lacourt, F. Courvoisier, and J. M. Dudley, "Soliton spectral tunnelling in photonic crystal fibre with sub-wavelength core defect," Electron. Lett. **43**, 967–968 (2007).
19. S. Stark, F. Biancalana, A. Podlipensky, and P. St. J. Russell, "Nonlinear wavelength conversion in photonic crystal fibers with three zero-dispersion points," Phys. Rev. A **83**, 023808 (2011).
20. S. J. Madden, D. Y. Choi, D. A. Bulla, A. V. Rode, B. Luther-Davies, V. G. Ta'eed, M. D. Pelusi, and B. J. Eggleton, "Long, low loss etched As_2S_3 chalcogenide waveguides for all-optical signal regeneration," Opt. Express **15**, 14414–14421 (2007).
21. X. Zeng, S. Ashihara, X. Chen, T. Shimura, and K. Kuroda, "Two-color pulse compression in aperiodically poled lithium niobate," Opt. Commun. **281**, 4499–4503 (2008).
22. N. E. Yu, J. H. Ro, M. Cha, S. Kurimura, and T. Taira, "Broadband quasi-phase-matched second-harmonic generation in MgO-doped periodically poled $LiNbO_3$ at the communications band," Opt. Lett. **27**, 1046–1048 (2002).

1. Introduction

Optical Cherenkov radiation (OCR), also referred to as dispersive wave generation or non-solitonic radiation, originates from soliton propagation perturbed by high order dispersion (HOD). The OCR becomes of particular importance in the octave-spanning spectral broadening and blue-shifted supercontinuum generation (SCG) [1–4]. The radiation wavelengths are determined by a phase-matching (PM) condition, requiring an identical phase velocity for the soliton and the radiations. Up to now, considerable efforts have been devoted to investigating the OCRs with the advent of photonic crystal fibers (PCFs) for their flexible dispersions and highly nonlinear properties [5, 6]. Most OCRs have been widely explored based on the dispersion profiles with one or two zero-dispersion wavelengths (ZDWs), in which the resonant radiations usually fall into the normal group velocity dispersion (GVD) region.

Chromatic dispersion influences the OCR frequencies through the PM condition [7, 8]: $\beta_s(\omega_r) = \beta(\omega_r)$, where $\beta_s(\omega) \equiv \beta(\omega_p) + \beta^{(1)}(\omega - \omega_p) + \gamma \cdot P/2$ reflects the nondispersive nature of a soliton, $\beta(\omega_j)$ is the frequency dependent propagation constant and $\beta^n(\omega_j)$ is n-th order derivative of β at ω_j, $j = r$ or p represents the radiation or pump wave. P denotes the peak power of the input pump soliton and γ is the nonlinear waveguide coefficient. Typically, OCRs are located at some discrete frequencies owing to the fact that β_s is a linear function of frequency (that is why soliton is non-dispersive).

In this paper, we investigate near-infrared OCRs in an As_2S_3 slot subwavelength waveguide by engineering its dispersion, and present a numerical analysis of a broadband radiation due to a zero group-velocity (GV) mismatch and broadband phase-matched nonlinear process. The mechanisms of narrow and broadband OCRs are studied in detail and excellent agreements between the PM predictions and numerical simulations are demonstrated. The proposed approach of minimizing the temporal walk-off between the pump soliton and the emitted radiation offers a general understanding of the OCR. Broadband OCR can serve as a new wavelength conversion scheme to achieve large conversion spanning. More important, it tends to a stable soliton state upon propagation, distinguished from linear radiations in the blue edge of the SCG. The broadband OCR may enhance the red edge of the SCG in the chalcogenide waveguide [9].

As$_2$S$_3$ material has a large Raman gain coefficient [10], a large Kerr nonlinear index $n_2 = 3.0 \times 10^{-18} m^2/W$, a high refractive index ($n \approx 2.4$) at the telecommunication wavelengths, and a low two photon absorption coefficient $\beta_{TPA} = 6.2 \times 10^{-15} m/W$ [11], which is three orders of magnitude lower than that of silicon [12].

2. Phase matching conditions of As$_2$S$_3$ slot waveguides

We use the recently proposed slot waveguide structure with subwavelength dimensions from Ref. [13], shown in the inset of Fig. 1(a). The difference is that a silica slot is surrounded by two As$_2$S$_3$ layers, instead of silicon. As$_2$S$_3$ waveguides are in practice protected by using a coating layer of inorganic polymer glass (IPG) [9] or GeSbS is used as the cladding material with a lower refractive index ($n \approx 2.3$ at 1.55 μm). To be simple, we use the air outmost cladding to calculate the dispersion profiles. The substrate is a 4-μm-thick SiO$_2$. Because of high refractive index contrast between As$_2$S$_3$ and silica ($n \approx 1.44$ at 1.55 μm), the discontinuity of the electric field in the interface induces a high confinement factor in the nano-scale slot [14]. The field confinement in horizontal slot configuration is achieved for transverse-magnetic modes. On the other hand, the magnitude of waveguide dispersion of the slot waveguide can be as high as the material dispersion, thus total dispersion can be greatly tailored [15].
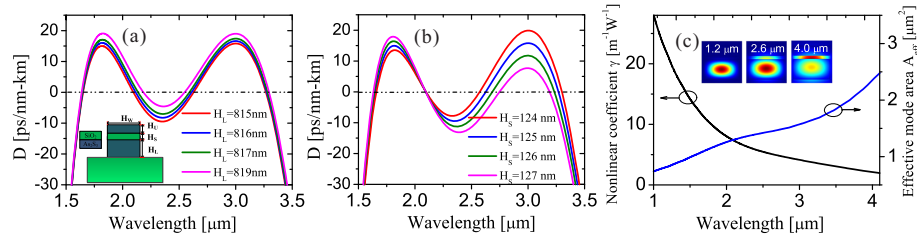

Fig. 1. Chromatic dispersion tailored by using different heights of (a) lower-layer As$_2$S$_3$ (H$_S$ = 125 nm) and (b) silica slot (H$_L$ = 815 nm). The inset in (a) is the structural geometry of an As$_2$S$_3$ slot waveguide. (c) Effective mode area and nonlinear coefficient vs. wavelength, and the insert in (c) is mode field distributions.

The structural parameters of the slot waveguide are set as: upper As$_2$S$_3$ height H$_U$ = 395 nm, slot height H$_S$ = 125 nm, waveguide width H$_W$ = 1400 nm and lower As$_2$S$_3$ height H$_L$ = 815 nm. The effective refractive index (n_{eff}) is calculated by employing the radio frequency module of the commercial COMSOL software. The total dispersion is then calculated by taking the 2nd-order derivative of n_{eff} with respect to the wavelength ($D = -(\lambda/c) d^2 n_{eff}/d\lambda^2$), where c and λ are the speed of light and the vacuum wavelength, respectively. A dispersion profile with four ZDWs is obtained as plotted in Fig. 1(a), where a normal GVD range is surrounded by two anomalous GVD regions. Formation of such a saddle-shaped dispersion profile is mainly due to the mode transition and anti-crossing effect [13] and the middle valley is lowered with a decreased H$_L$. As shown in Fig. 1(b), increasing silica height leads to the mode transition at longer wavelengths and thus the third ZDW becomes longer. Compared to As$_2$S$_3$ rib waveguide with two ZDWs [9], in which an anomalous GVD region is surrounded by two normal GVD regions, two anomalous GVD regions can be formed in the slot waveguide.

Note that it is important to consider the wavelength dependence of the nonlinear coefficient on the waveguide mode in the simulation of a broadband spectral evolution. We calculate the effective mode area A_{eff} and the nonlinear coefficient γ by using [16, 17]: $A_{eff} = \left(\iint |F(x,y)|^2 dxdy \right)^2 / \iint |F(x,y)|^4 dxdy$ and $\gamma = \left(\frac{2\pi}{\lambda} \iint \bar{n}_2(x,y)|F(x,y)|^4 dxdy + i \frac{\beta_{TPA}}{2} \right) / \left(\iint |F(x,y)|^2 dxdy \right)^2$, where $F(x,y)$ is mode field distribution and $\bar{n}_2(x,y)$ means the

nonlinear index distribution of the slot waveguide. Results shown in Fig. 1(c) indicate that the longer the wavelength, the larger the optical field area, and the smaller the induced nonlinear coefficients are.
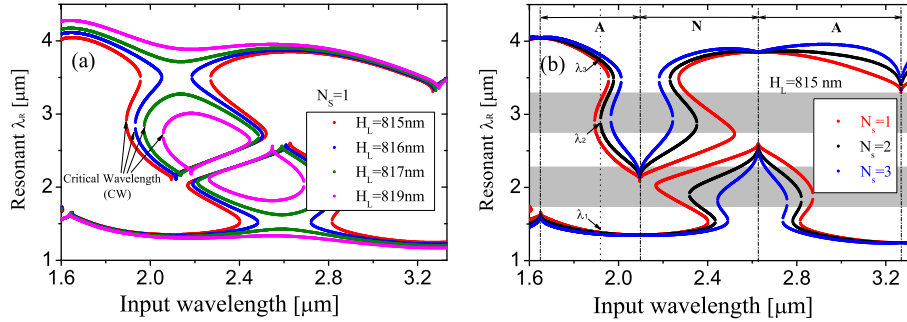

Fig. 2. (a) Phase-matching topologies ($N_S = 1$) corresponding to four dispersion profiles plotted in Fig. 1(a). (b) PM topologies (H_L =815 nm) with respect to the input N_S (the gray areas are anomalous GVD regions, A and N represent anomalous and normal GVD, respectively). The input pulse is 50 fs (FWHM) with a hyperbolic secant shape.

The PM topologies are shown in Fig. 2 within a wide span of both the soliton wavelength and the resonant OCR wavelength. It is obvious that different dispersion profiles have different PM topologies, As shown in Fig. 2(a), besides two radiation bands in the blue and red sides (around 1.5 μm and 3.5 μm), additional OCR bands are predicted due to the existence of the middle two ZDWs. The two middle OCR bands become degenerate at a critical wavelength (CW), labeled as λ_2 in Fig. 2(b), which is located in the anomalous GVD region. The OCR at the CW is always located in another anomalous GVD region, therefore propagating as a soliton state. This nonlinear process is known as soliton spectral tunneling effect [18, 19]. When having a higher order soliton number, the corresponding PM topologies are shown in Fig. 2(b), in which the OCR band slightly increases while red-shifting the CW.

3. Numerical results and discussion

We now study the behavior of ultrashort pulse propagation inside an As_2S_3 waveguide. A detailed analysis is provided, based on the numerical solution of the generalized nonlinear Schrödinger equation (GNLSE):

$$\frac{\partial A(z,T)}{\partial T} + \frac{\alpha}{2}A(z,T) = \mathscr{F}^{-1}\left\{\left[\beta(\omega) - \beta(\omega_0) - \beta^{(1)}(\omega_0)(\omega - \omega_0)\right]\tilde{A}(z,\omega)\right\}$$
$$+i\gamma\left(1 + \frac{i}{\omega_0}\frac{\partial}{\partial T}\right)A(z,T) \times \int_{-\infty}^{+\infty} R(T - T')|A(z,T')|^2 dT' \tag{1}$$

where the complex $A(z,T)$ is a time-domain description of the propagating field envelope in a reference frame traveling with the input pulse. The second term represents the linear loss α, which is assumed to be negligible in the simulation because of low loss propagating in the As_2S_3 [20] and less power distribution in silica slot for shorter wavelengths than 3 μm. In the right-hand side, the term with a integral denotes the 3-order nonlinear wave interaction through the material Raman response, where $R(t) = (1 - f_R)\delta(t) + f_R h_R(t)$ is the nonlinear response function of As_2S_3 waveguide and h_R is taken as $h_R(t) = \frac{\tau_1^2 + \tau_2^2}{\tau_1 \tau_2^2}\exp\left(-\frac{t}{\tau_2}\right)\sin\left(\frac{t}{\tau_1}\right)$, where τ_1 is 15.5 fs, τ_2 is 230.5 fs and the Raman ratio f_R is 0.1 [10]. All HOD terms and the wavelength dependent nonlinear coefficient are included in the simulations.
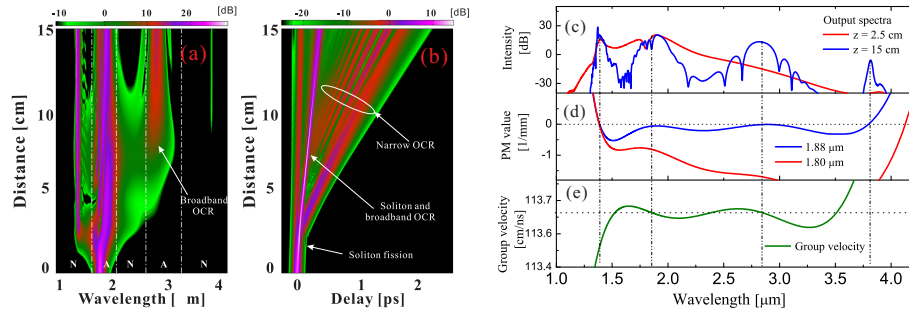
Fig. 3. (a) Spectral and (b) temporal dynamics of 50 fs input soliton ($N_S = 2$) at the wavelength of 1.8 μm in As$_2$S$_3$ slot waveguide, A and N represent anomalous and normal GVD. (c) Spectrum at the soliton fission (red line) and the output (blue line). (d) PM $\equiv \beta_s(\lambda_p) - \beta(\lambda)$ curves at the different soliton wavelengths λ_p and (e) GV curve.

Figure 3(a, b) show the spectral and temporal evolution dynamics of the soliton in such an As$_2$S$_3$ slot waveguide with four ZDWs. The dispersion profile used in the simulation is the red line in Fig. 1(a) and its corresponding PM curve is the black line in Fig. 2(b). We launch a 50 fs pulse (FWHM: full width at half maximum) at the central wavelength of 1.8 μm into a 15-cm long As$_2$S$_3$ slot waveguide. Its soliton number $N_S = 2$ requires the pump power of 12.80 W. The soliton fission occurs at the propagating distance ($z = 2.5$ cm), where a predicted narrow-band OCR is detached at the wavelength of 1.39 μm. The spectrum after the soliton fission is shown in Fig. 3(c). The narrow PM condition is shown in the red curve of Fig. 3(d) and large GV mismatch is seen in Fig. 3(e). The GV is defined as $v_g = 1/\beta^{(1)}$ and the GV-mismatch parameter is $d_{12} = 1/v_g(\omega_p) - 1/v_g(\omega_r)$. This narrow-band OCR quickly becomes separated and delayed from the main pulse. A streak in the temporal evolution is clearly shown in Fig. 3(b).
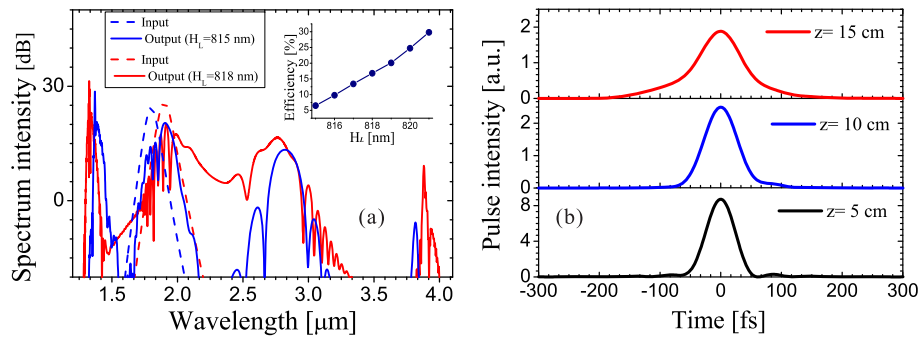

Fig. 4. (a) Output spectra intensities under the different dispersion profiles (the inset is the OCR conversion efficiency vs. H_L). (b) Pulse intensities of the OCR by filtering away the spectrum shorter than 2.25 μm (under the dispersion profiles $H_L = 815$ nm).

When the pump soliton approaches the CW (1.88 μm) due to the soliton self-frequency shift (SSFS) induced by the Raman effect, the second phase-matched OCR band located at $\lambda_2 = 2.83$ μm is observed with a broad bandwidth as shown in Fig. 3(c). It is found that the radiation has the same GV as the pump soliton at the CW in Fig. 3(e). Thus GV matching results in a broad conversion band at the wavelength of 2.83 μm. The third narrow OCR band located in 3.81 μm is too weak because it is far away from the pump soliton.

The mechanisms behind narrow and broadband OCRs are easily understood by recalling the broadband second harmonic generation (SHG) in $\chi^{(2)}$ media [21, 22]. The SHG bandwidth $\Delta\lambda$ is determined by the width of $\mathrm{sinc}^2(\Delta\beta L/2)$ and the efficiency is proportional to the interaction length L, assuming an undepleted fundamental and neglecting temporal dispersion. Therefore we need to minimize the phase mismatch $\Delta\beta$, i.e., $\Delta\beta \approx \Delta\beta(\lambda_0) + \frac{\partial(\Delta\beta)}{\partial\lambda}(\lambda - \lambda_0) + \frac{1}{2}\frac{\partial^2(\Delta\beta)}{\partial\lambda^2}(\lambda - \lambda_0)^2$, and $\frac{\partial(\Delta\beta)}{\partial\lambda} = \frac{4\pi c}{\lambda^2}d_{12}$ indicates larger conversion bandwidths when GV matching between the radiation and the soliton. The OCR efficiency is determined by the spectral overlap between the pump soliton and the radiation. As shown in Fig. 4(a), the OCR efficiency is increased as H_L increases, in which the wavelength span between the CW and its radiation decreases as seen in Fig. 2(a). More important, the broadband OCR tends to a stable soliton state in the anomalous GVD region upon propagation, as shown in Fig. 4(b).
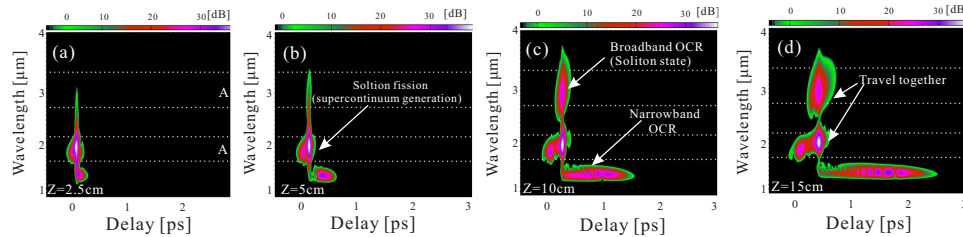

Fig. 5. Pulse spectrograms at (a) 2.5-cm (b) 5-cm (c) 10-cm and (d) 15-cm distance.

The soliton evolution dynamics mentioned above are also confirmed by using the spectrogram in Fig. 5, in which the pulses are depicted simultaneously in the temporal and spectral domains. The spectrogram is calculated by $S(\lambda,\tau,z) = \left|\int_{-\infty}^{+\infty} E(z,t)\,g(t-\tau)\exp\left(-i\frac{2\pi c}{\lambda}t\right)dt\right|^2$, where $g(t-\tau)$ is the variable delay gate function with a delay value τ. With a propagation length $z = 2.5$ cm, an OCR band first appears in the short wavelength (around 1.39 μm), see Fig. 5(a). Upon further propagation, a tail-like shape in the spectrogram is formed due to large GV mismatch between the soliton and the first OCR. When the soliton pulse is red-shifted to approach the CW, the soliton spectrum becomes broadened over the normal GVD regime as shown in Fig. 5(b) and a broadband OCR at 2.83 μm is GV matching to the soliton pulse. Then this OCR grows up quickly, see Fig. 5(c). Afterwards, the second broadband OCR forms a soliton state as shown in Fig. 5(d).

4. Conclusion

We demonstrate an efficient broadband OCR in an As_2S_3 slot waveguide with four ZDWs. The presence of multiple ZDWs presents different PM topologies for the OCR. A broadband PM nonlinear process is found at the CW, where the soliton and the resonant radiation are GV matched. We make a detailed description of the OCR processes and numerical simulations clearly show the mechanisms of narrow and broadband OCRs by using the spectral evolution and the spectrogram. The broadband OCR investigated in the chalcogenide waveguide is expected to generate near-IR optical source as a new wavelength conversion scheme.

Acknowledgments